International Journal of Nanoelectronics and Materials

In Press, Accepted Manuscript – Note to user

Synthesis of Sustainable Binary Calcium Monosilicate Ceramics from Bio-waste: Effect of Sintering Temperature on Microstructure and Electrical Properties

N. H. Jakfar[3], S. F. Khor [1,2*], B. Johar[3], N. M. S. Adzali[3], S. N. H. Mohd. Yunus[2], E. M. Cheng[4,5], E. Z. M. Tarmizi[6], Z. A. Talib[7]

[1] Centre of Excellence for Renewable Energy (CERE), Universiti Malaysia Perlis (UniMAP), Perlis, Malaysia.
[2] Faculty of Electrical Engineering Technology, Universiti Malaysia Perlis (UniMAP), Perlis, Malaysia.
[3] Faculty of Chemical Engineering Technology, Universiti Malaysia Perlis (UniMAP), Perlis, Malaysia.
[4] Advanced Communication Engineering, Centre of Excellence (ACE), Universiti Malaysia Perlis (UniMAP), Perlis, Malaysia.
[5] Faculty of Electronic Engineering Technology, Universiti Malaysia Perlis (UniMAP), Perlis, Malaysia.
[6] Centre of Foundation Studies for Agricultural Science, Universiti Putra Malaysia UPM, 43400, Serdang, Selangor, Malaysia.
[7] Department of Physics, College of Natural Sciences, Jeonbuk National University 567, Baekje-daero, Deokjin-gu, Jeonju-si, Jeollabuk-do, 54896 Republic of Korea.

Received 28 April 2022, Revised 15 June 2022, Accepted 4 July 2022

ABSTRACT

This study was conducted to synthesise calcium monosilicate ceramics using rice husks and raw eggshells and investigated the effect of sintering temperature on the physical, microstructure and electrical properties of the final product. The high content of calcium and silicon in eggshells and rice husks, respectively promote the use of waste materials in the production of calcium monosilicates by mixing in a molar ratio 1CaO:1SiO$_2$ and fired at different sintering temperatures for 2 hours with a heating rate of 10°C/min. A good correlation between sintering temperature, structural, microstructure, and electrical properties of calcium silicate was observed. The structural and morphological evolution were characterised by X-ray diffraction (XRD) and scanning electron microscopy (SEM) equipped with electron dispersive X-ray analysis (EDX). XRD analysis showed that the main crystalline phases of synthesised calcium monosilicate are pseudowollastonite (ICSD 98-005-2598) at 1250°C, and the phases of SiO$_2$ also exist in different types of minerals. Besides, a small amount of larnite, Ca$_2$SiO$_4$ was traced at 1100°C and 1200°C. Fourier Transforms Infrared (FTIR) spectra showed the presence of characteristic functional groups in the precursor powder. In Nyquist plots, the summit frequency of the dominant arc decreases with increasing sintering temperatures. It may be attributed to the co-effect of the grain size and pore. A larger value of impedance at a lower frequency suggests an essential role of boundaries in governing the electrical properties of the sintered ceramics. As the sintering temperature increases, the microstructure of the sintered samples becomes denser while conductivity performance decreases. This is due to the reduction of particle interfaces and charge transfer.

Keywords: Calcium monosilicate, Sintering, Electrical conductivity, Impedance

* sfkhor@unimap.edu.my

Note: Accepted manuscripts are articles that have been peer-reviewed and accepted for publication by the Editorial Board. These articles have not yet been copyedited and/or formatted in the journal house style.

1. INTRODUCTION

Calcium monosilicate is one of the naturally occurring mineral materials or is commercially prepared from binary CaO-SiO_2 system materials, such as limestone, quartz, and others. However, calcium silicate ceramics can be fabricated and derived from agriculture and food by-product or waste rich in silica and calcium carbonate components [1, 2]. The rational use of residues by controlling the combustion process can increase its value and release the pressure on nature, making it a valuable resource for materials science. This is because it can provide cheap, renewable, and environmentally friendly materials and development technologies [3, 4]. In reality, less commercial interest and neglected mineral value render the waste discarded either burnt, dumped as waste, or utilised for non-energy-related low-value applications. The current practice of disposing of food and agricultural biodegradable wastes at landfills is not sustainable as it depletes the limited landfill space, creates hygiene problems, and squanders the valuable mineral contents.

Therefore, nowadays, the uses of waste are favourable in producing types of materials. Producing of calcium silicates is mainly studied in the SiO_2 - CaO system, which is used to produce thermal insulator ceramic material [1], cement industries, and biomedical industries. The potential waste materials that can synthesise calcium monosilicate are rice husks and eggshells because they can produce silica and calcium oxide, respectively. Extraction of silica from rice husk would be a cost-effective process as it gives a high silica content [5]. On the other hand, eggshells are chiefly composed of calcium carbonate and decomposed to calcium oxide at high temperatures [6].

Several studies have reported the decomposition of rice husk and eggshells. Haslinawati et al. [7] extracted silica from rice husk at 500°C and calcined it at 800°C for 2 hours for complete combustion. T. Zaman et al. [8] calcined the eggshells in a muffle furnace at a temperature within 800°C-1000°C with 2 hours of soaking time. Both calcined powders contained a mixture of lime and portlandite phases in eggshells [8] while the amorphous phase for silica in rice husk [9].

This work aims to study the feasibility of producing valuable calcium monosilicate using silica and calcium oxide sources derived from bio-wastes, i.e., rice husk and eggshell powder. Besides, the effect of sintering temperature on the structural, morphological and electrical properties of synthesised calcium monosilicate was investigated. Generally, calcium monosilicate is synthesized at very high temperatures within 1300°C to 1500°C. Tangboriboon et al. [10] reported that β-calcium silicate can be formed at 870°C and further transformed into α-calcium silicate at 1125°C. However, the present work successfully synthesised α-calcium silicate, i.e., pseudowollastonite (ICSD 98-005-2598) at 1250°C. However, a highly dense calcium monosilicate is difficult to obtain because its grains grew exceptionally and become more porous with increasing sintering temperature. In the present work, the used powder material has been characterised by mineralogical composition X-ray diffraction, Fourier transform infrared spectroscopy, and X-ray fluorescence. The sintered synthesised $CaSiO_3$ undergoes X-ray diffraction and microstructural analysis, density and porosity analysis using Archimedes principle, and impedance analysis. These findings show the intricate interactions between microstructure, morphology, and transport properties, emphasizing the importance of dielectric materials design for industrial applications.

2. MATERIAL AND METHODS

Raw rice husks were obtained from a rice mill factory in the North region of Malaysia and eggshells from the daily basis of food waste were used as raw materials. Both of the materials were cleaned and dried before the calcination process. Rice husks were calcined at temperature 800°C for 2 hours, while raw eggshells were calcined at temperature 900°C for 4 hours at a heating rate of 10°C/min. White powder material was then obtained from both raw materials.

The chemical composition of the white powder materials was determined by Energy Dispersive X-ray Fluorescence (EDXRF, PAN analytical MiniPAL 4) technique. The functional groups that existed in the samples powder were determined by Fourier transform infrared (FTIR) analysis. The FTIR spectra were obtained in transmittance mode from 600 cm^{-1} – 4000 cm^{-1} at a resolution of 1 cm^{-1} using a Perkin Elmer FTIR spectrum RXI spectrometer.

Samples of calcium monosilicates formulation were prepared by mixing the powder of calcined rice husk and calcined eggshell with ratio $CaO:SiO_2$ (1:1) through mortar and pestle. Then, the mixed powder was shaped in a cylindrical pellet with a dimension of 13 mm diameter and 2 mm thickness by using a hand pressing tool with 2 tonnes of pressure. Next, the shaped pellets were sintered at various temperatures (1100°C, 1150°C, 1200°C, and 1250°C) for 2 hours with a heating rate of 10°C/min.

Phase analyses of the pre-sintered and sintered samples were performed by X-ray diffraction (XRD: Bruker D2 Phaser Model) operating from 5° to 90° 2θ at a scan speed of 2° 2θ/min and a step size of 0.02° 2θ with CuK_α radiation (K_α = 1.5406 nm) at 10 mA and 30 kV. Identification of phases was achieved by comparing the result diffraction patterns with the ICSD (JCPDS) standard. Xpert-Highscore Plus software was used.

The microstructure and morphology of the sintered samples were observed by a scanning electron microscope (SEM: JEOL JSM-6450LA) coupled with an energy-dispersive X-ray (EDX) spectrometer. The samples were platinum-coated by spin coating technique and mounted on the SEM sample stage with conductive double-sided carbon tape before SEM imaging. The images were taken at different magnifications (2000X and 500X) to allow the multiscale perception of the features present in the sintered samples following prescribed heat treatment.

The Archimedes principle was applied to determine the densification and porosity of the samples. This procedure was carried out using the standard test method of ISO 5017, ASTM C20, and BS 1902-308 [11]. On the other hand, the percentage of linear shrinkage was calculated using the following expression

$$\text{Shrinkage (\%)} = [(L_o - L)/L_o] \times 100 \quad (1)$$

where L_o and L are the length of the sample specimen before and after the sintering process, respectively [12].

Impedance measurements were carried out by using an impedance analyzer (IM3570, Hioki, Japan with a L2000 4-terminals probe) at the oscillation voltage of 1 V, in the frequency range of 4 Hz to 5 MHz. The measurements were performed over the temperature ranging from 200°C to 300°C.

3. RESULTS AND DISCUSSION

3.1 Characterisation of powder material

The result of XRF analysis for calcined rice husk (RHA) and calcined eggshell (CES) powders is tabulated in Table 1. The highest content element in RHA and CES is silicon dioxide (SiO_2) and calcium oxide (CaO), accounting for 91.7% and 96.23% of the composition, respectively. In other words, the RHA and CES are silica and calcium-rich wastes, respectively. Since natural materials are used as precursors, other elements are also present in powders with a low percentage.

Table 1 Percentage of chemical compositions exist in RHA and CES.

RHA		CES	
Element	%	**Element**	%
SiO_2	91.7	**CaO**	96.23
K_2O	5.88	**Na_2O**	2.40
CaO	1.58	**MgO**	0.58
MnO	0.252	**Al_2O_3**	0.20
Fe_2O_3	0.171	**RuO_2**	0.20
CuO	0.067	**SO_3**	0.10
ZnO	0.043	**Nd_2O_3**	0.10
As_2O_2	0.006	**Cu_3O_4**	0.08
Rb_2O	0.018	**SrO**	0.058
PdO	0.12	**CuO**	0.032
Eu_2O_3	0.070	**Sm_2O_3**	0.03
Re_2O_7	0.037	**Yb_2O_3**	0.03
OsO_4	0.009	**ZrO_2**	0.015
PbO	0.02		

Figure 1 shows FTIR spectrum at the wavenumber of 600 cm^{-1} – 4000 cm^{-1} for RHA after calcined at 800°C. The spectrum has two prominent peaks located at 1045 cm^{-1} and 796 cm^{-1} which are attributed to the vibration mode of Si-O-Si [13]. The peak at 1045 cm^{-1} is characteristic of Si-O-Si amorphous silica and is confirmed by the presence of a broad hump structure between 15 and 30 (2θ) on the X-ray pattern of RHA. On the other hand, the FTIR spectra in Figure 2 show the effect of calcination on functional groups of eggshells. There is an intense transmittance band of ES at 1399 cm^{-1}. It is corresponds to the elongation modes of C-O bonds of calcite [13,14]. Besides, two peaks present at 705 cm^{-1} and 868 cm^{-1} indicate the existence of calcium carbonate [13,14,15]. For CES, there are no significant transmittance peaks. It denotes that the basic components of eggshells, i.e., $CaCO_3$, are no longer present [13]. However, CES with lower intensity bands reveals that the calcite is still not completely decomposed during the calcination process, and the peak at 1423.39 cm^{-1} is associated with the C-O bond of CO_3 group of eggshells [16]. Despite the decrement of intensity, a new sharp peak is observed at 3632 cm^{-1} of the CES, indicating the O-H stretching vibration of $Ca(OH)_2$. The formation of $Ca(OH)_2$ is due to successive decarbonisation and hydration reactions, as shown in Equations (2) and (3). $CaCO_3$ decomposed to form CaO and CO_2 upon calcination, and then the active CaO was hydrated by moisture from the atmosphere to form $Ca(OH)_2$, which could not be prevented or avoided.

$$CaCO_3\,(s) + \text{energy} \rightarrow CaO\,(s) + CO_2\,(g) \qquad (2)$$

$CaO (s) + H_2O (g) \rightarrow Ca(OH)_2 (s)$ (3)

In addition, there are several dips in the spectrum within 2352.40 cm^{-1} and 2023.79 cm^{-1} representing the presence of atmospheric CO_2 [17, 18]. The presence of these peaks probably related to poor background collection and can be related to the calcination process of $CaCO_3$, which produced active CaO that also capture CO_2 during combustion or gasification [19, 20].

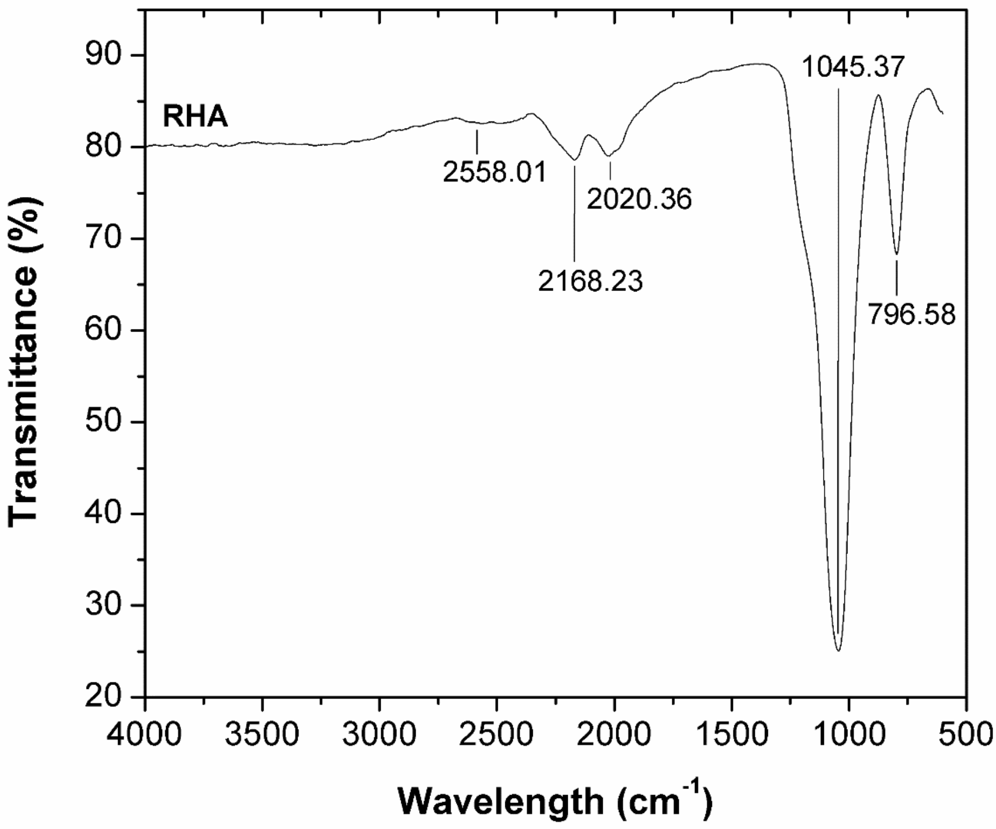

Figure 1. FTIR result of calcined rice husk.

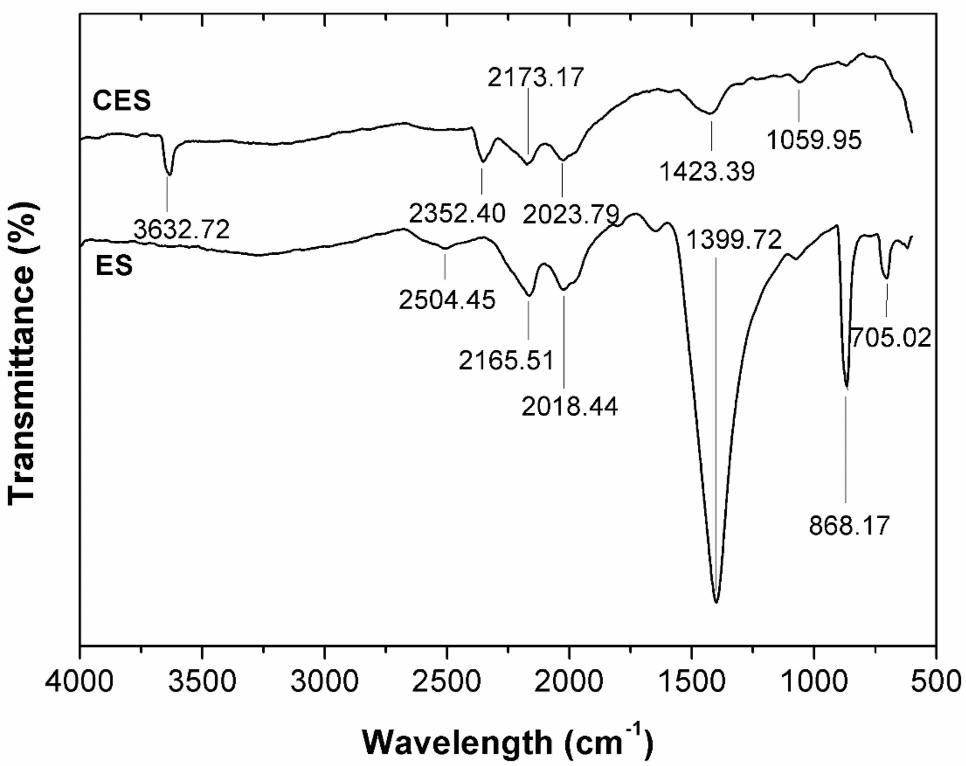

Figure 2. FTIR result of raw eggshell and calcined eggshell.

Figure 3 shows the XRD pattern for calcined rice husk and calcined eggshells. The characterisation is using 2θ range of 5° to 90°. The XRD pattern of RHA sample shows a broad diffraction pattern of SiO_2 with only one phase with the highest intensity at 21.87°, indicating high percentages of amorphous phases. Also, there are no other defined peaks were observed. Meanwhile, the XRD pattern for CES presents the peak of calcium oxide (CaO) at 2θ of 32.173° (111), 37.321° (002), 53.807° (002), 64.091° (113), 67.309° (113), 79.571° (004), and 88.427° (133). Besides, the calcium oxide phase portlandite ($Ca(OH)_2$) was also observed at 2θ – 17.956° (001), 33.997° (001), 46.926° (012), and 50.705° (133). Calcium carbonate ($CaCO_3$) present in the CES may ascribe to the incomplete decomposition of $CaCO_3$ in raw eggshells during the calcination process. The cycle of calcination and carbonation reaction is shown in Equation (4):

$$CaO\ (s) + CO_2\ (g) \rightarrow CaCO_3\ (s) \qquad (4)$$

The forward reaction is exothermic (-178 kJ/mol), whereas the reverse reaction is endothermic (178 kJ/mol), which is referred the calcination reaction [19, 20]. The actual rate of the reaction depends on the reaction mechanism, temperature, and accessibility of the solid reactants.

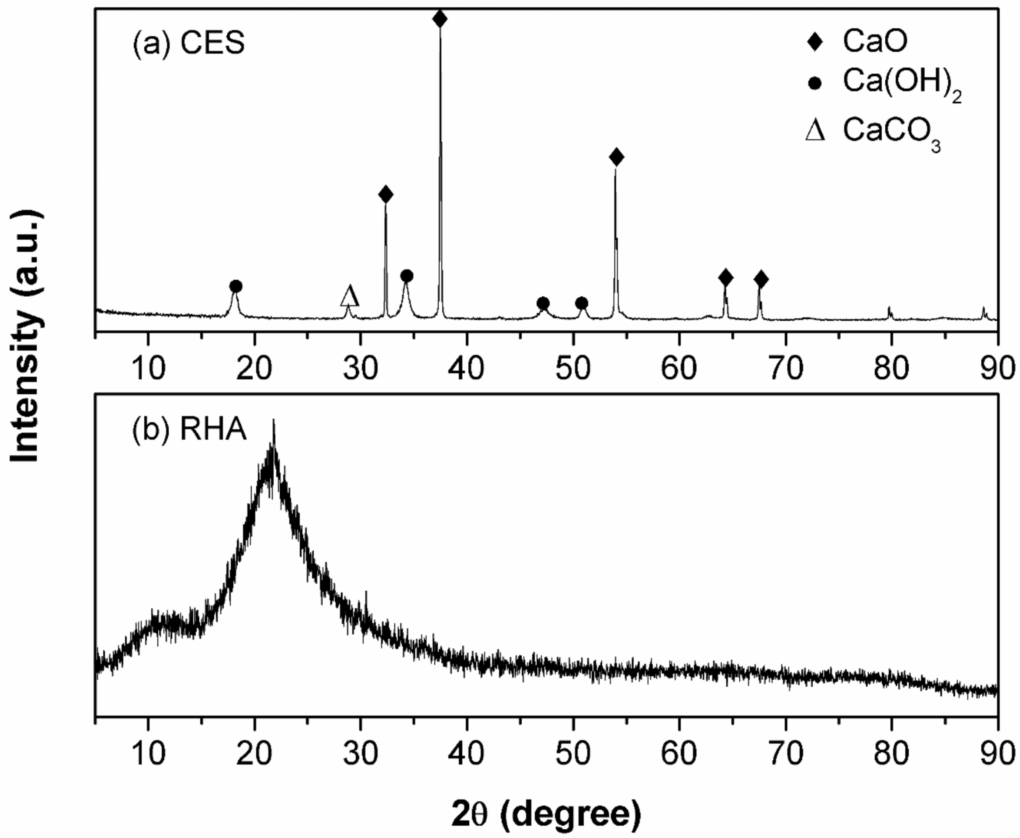

Figure 3. XRD result of calcined rice husk and calcined eggshell.

3.2 Characterisation of sintered samples

Compact ceramic powder undergoes several major changes during the sintering process, including solid-state chemical reactions such as decomposition, oxidation, and phase transformation. The XRD pattern of synthesised calcium monosilicate ceramics is shown in Figure 4. The result clearly shows that all the studied formulations have a similar pattern phase transformation, and the intensity peak increases with increasing temperature. The increase of the intensity peak indicates that the temperature affects the crystallization reaction during the sintering process and leads to higher densification of the sample with accompanying morphological changes. When the temperature increases to 1250°C, the main crystalline phase is pseudowollastonite (ICSD 98-005-2598), which is in the monoclinic phase with the following unit cell: a – 6.8390; b – 11.8700; c – 19.6310; α = 90.000; β = 90.000; and γ = 90.00. Moreover, other phases of SiO_2 also exist in different types of minerals, namely cristobalite beta high (ICSD 98-006-1840), cristobalite beta low (ICSD 98-006-0930), cristobalite beta low (98-003-4651)) and cristobalite beta high (ICSD 98-006-1839), relative to 1100°C, 1150°C, 1200°C and 1250°C. Besides, a small amount of larnite, Ca_2SiO_4 and carbon was also traced at 1100°C, 1200°C, and 1250°C.

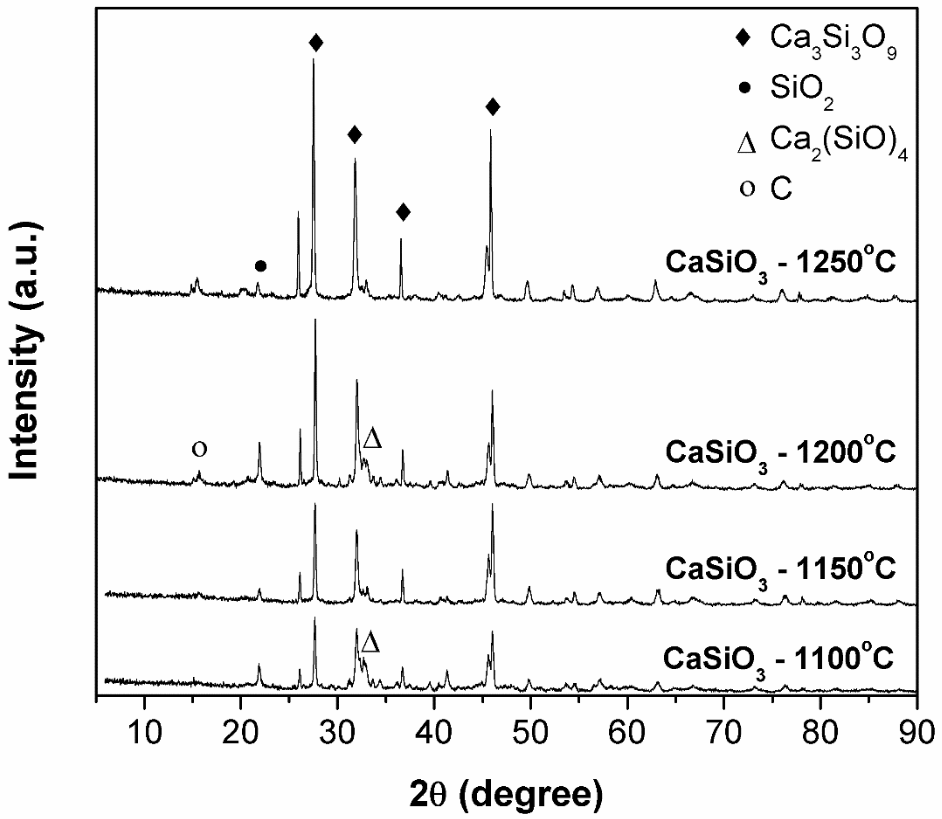

Figure 4. XRD result of sintered samples at different sintering temperatures

The XRD intensity peaks increase with sintering temperature is related to the morphological change, which is caused by the collapse of the mineralized framework and the sample's shrinkage, thereby leading to densification [21]. The statement is supported by density measurement. The empirical result of bulk density for the sintered calcium silicates increased with sintering temperature, as shown in Figure 5. The bulk density is 1.260 g/cm^3, 1.260 g/cm^3, 1.294 g/cm^3 and 1.375 g/cm^3 for 1100°C, 1150°C, 1200°C and 1250°C, respectively, which is in agreement with the results of XRD. It is thus concluded that the highest density was reached at a temperature of 1250°C. Despite the rise in bulk density, only 62.5% densification was attained at 1250°C. The density is just 47% that of natural calcium silicate (2.91 g/cm^3). Figure 5 also clearly shows that the shrinkage rate of the samples also increased with the sintering temperature. The pellet thickness decreases with the sintering temperatures due to the shrinkage, and such phenomena generally occurred during the high-temperature sintering [22, 23]. Also, the percentage of porosity is 47.2%, 47.2%, 44.1% and 37.5% for 1100°C, 1150°C, 1200°C and 1250°C, respectively. In short, the higher the shrinkage rate, the lower the porosity percentage and the greater the densification percentage. However, more research is needed to increase densification. It is due to high densification can directly improve mechanical properties such as hardness and strength, making it suitable for industrial applications.

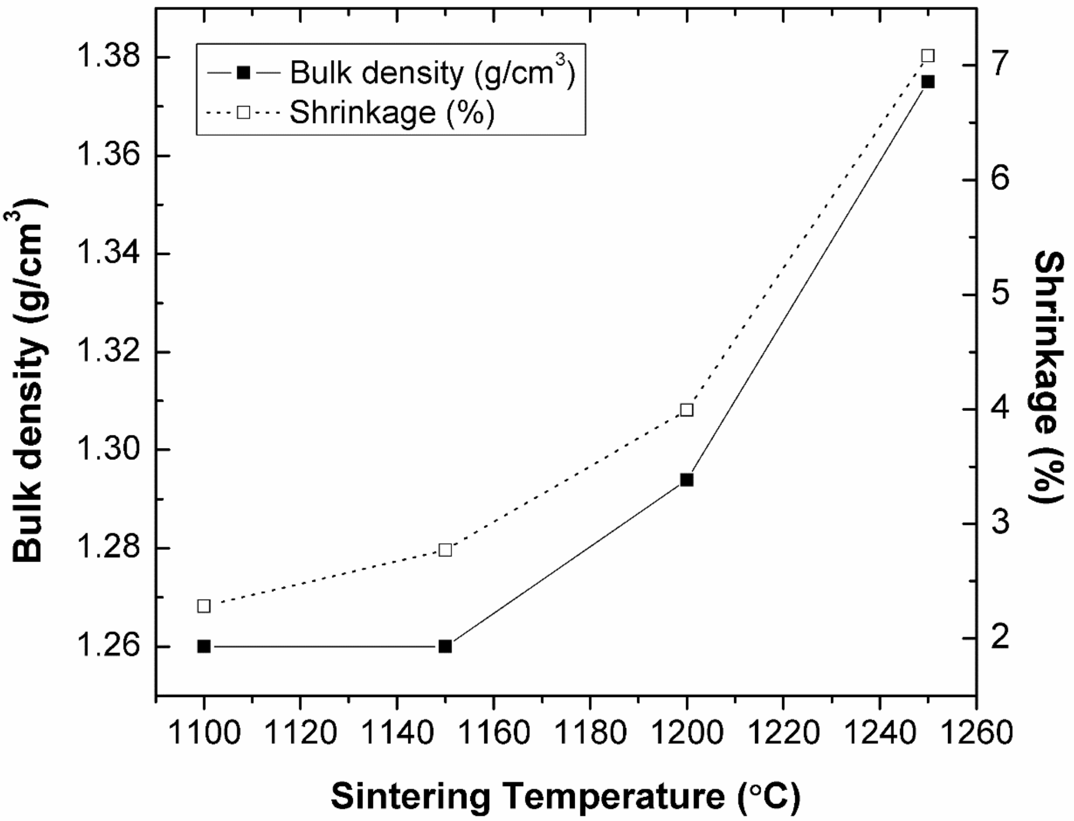

Figure 5. The effect of sintering temperatures on density and shrinkage.

Sintering is a process to provide the energy to the ceramic powder particle to bond together to remove the porosity from compaction stages resulting in a crystalline structure. The morphology of calcium monosilicate samples sintered at different temperatures was examined, and SEM micrographs of the sample surfaces are shown in Figure 6. Micrographs for all the sintered samples show that the grains with irregular morphology are non-uniformly distributed with multiple grain boundaries and porous microstructure. These characteristics in microstructure are governed due to the matter transportation mechanism during the solid-state reaction [24]. According to Figure 6a(i), the 1100°C pellet shows that the sample consists of well-necked particles with a wide size distribution. It is because the used powder was simply grounded by pestle and mortar without further control on particle size. The microstructure changes slightly for subsequent calcium monosilicate sintering at higher temperatures as the size distribution becomes narrow, and it forms a larger void distance around the grain boundaries and grain growth. As the sintering temperature increases to 1250°C, the microstructure develops a greater interlocking structure in three dimensions to form larger clusters and more consolidated. In other words, the pellet has formed a bulk structure with a higher density compared to the pellets sintered at 1100°C. The particle shape of the sample was destroyed when sintered at 1250°C. This leads to a significant decrease in the specific area and particle interfaces that can provide transport pathways for ionic conduction [25]. Also, the void distances widen around the grain boundaries hindering the flow of charge carriers by reducing the conduction path [26, 27]. Such structural proves the decrease in electrical conductivity as the trapped charge density increases. Besides, the morphological changes caused by sintering are accompanied by a change in phase composition, as discussed in X-ray diffraction data analysis [21].

The energy dispersive X-ray (EDX) analysis was employed over the surface area of the sintered sample at 1250°C. Figure 7 depicts the EDX line spectrum of the light and dark area on the surface of the corresponding SEM image. Both spectrums highlight the presence of silicon (Si), calcium (Ca), oxygen (O), and carbon (C) residing on the surface. These results are also in agreement with chemical composition and XRD patterns. Within the detection limit of EDX, we do not observe any metal clustering in the sample.

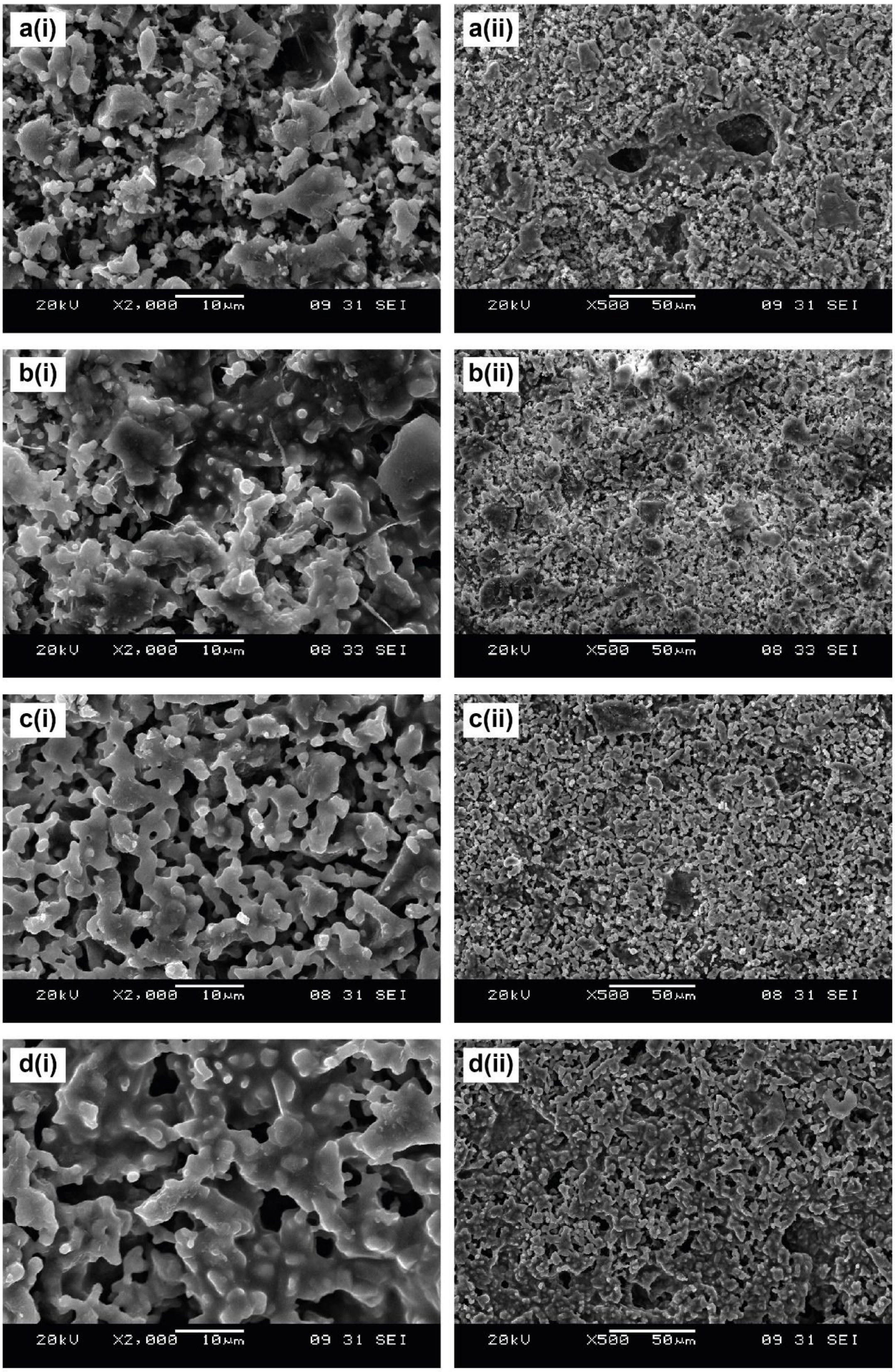
a(i)
20kV X2,000 10µm 09 31 SEI
a(ii)
20kV X500 50µm 09 31 SEI
b(i)
20kV X2,000 10µm 08 33 SEI
b(ii)
20kV X500 50µm 08 33 SEI
c(i)
20kV X2,000 10µm 08 31 SEI
c(ii)
20kV X500 50µm 08 31 SEI
d(i)
20kV X2,000 10µm 09 31 SEI
d(ii)
20kV X500 50µm 09 31 SEI

Figure 6. The morphology of sintered $CaSiO_3$ samples with X2000 magnification at (a)i) 1100°C, (b)i) 1150°C, (c)i) 1200°C (d)i) 1250°C, and with X500 magnification at (a)ii) 1100°C, (b)ii) 1150°C, (c)ii) 1200°C, (d)ii) 1250°C.

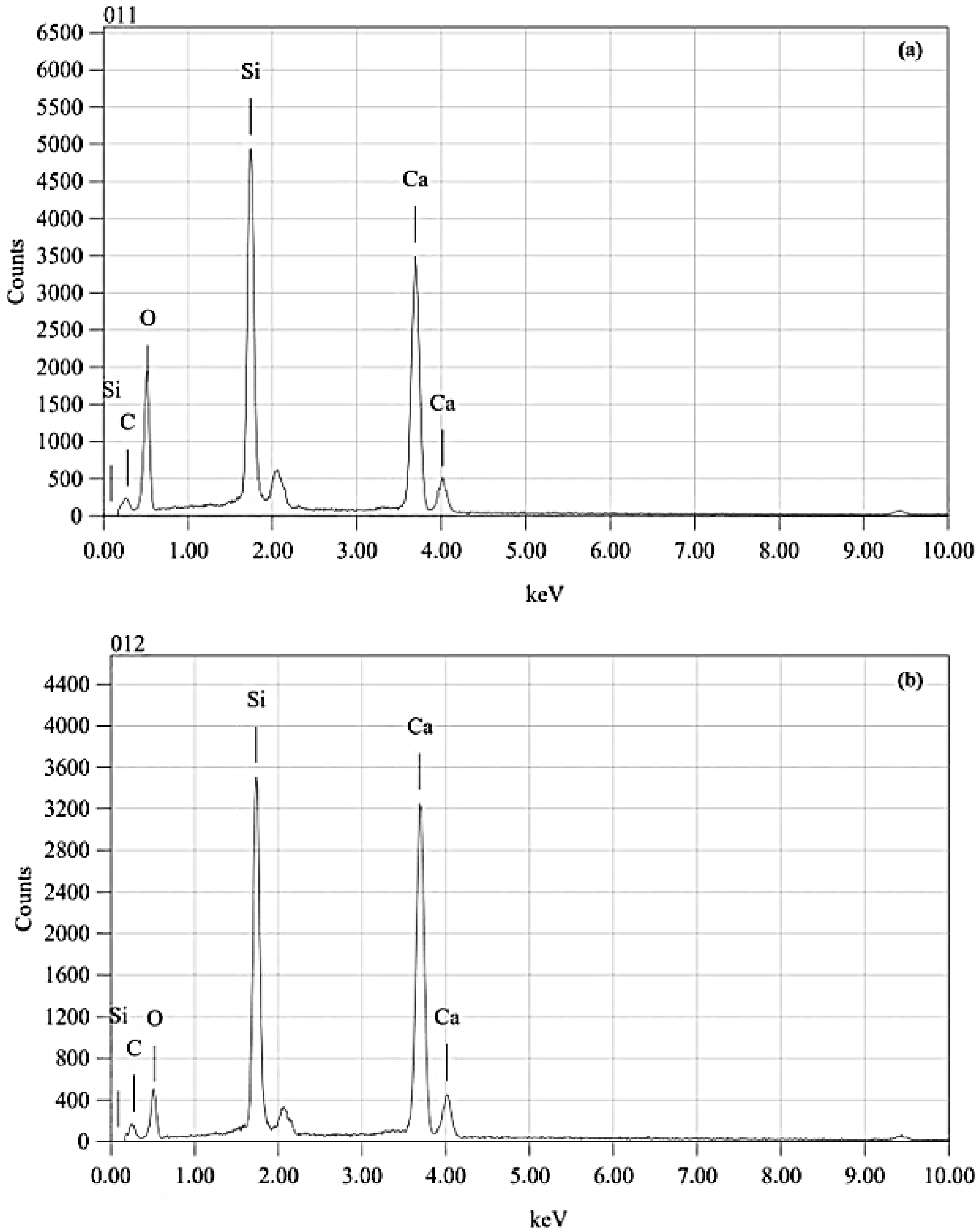

Figure 7. EDX spectrum from a (a) light and (b) dark area of the sample sintered at 1250°C.

Impedance analysis is a valuable tool to reveal the electrical conducting nature properties of samples, for instance, the impact of grain, grain boundary parameters, and also electrode effect or interfaces effect of the sample through separate capacitive and resistive contributions arising from grains, grain-boundaries and electrode-specimen interface. The complex impedance Z* of the network is defined as:

$$Z^*(\omega) = Z'(\omega) - jZ''(\omega) \quad (5)$$

Where Z' is the real part and Z'' the imaginary part of the complex impedance.

Figure 8 shows the Nyquist plots of the pellets sintered at different temperatures. As seen from the figure, the center of the semicircle is depressed below the real axis of impedance due to defects, structural stresses and distributed elements present in the system [28], indicating a non-Debye in nature [29, 30]. Besides, the absence of a tail in the low-frequency range indicates no ion blocking electrode. Generally, the first semicircle at high frequencies could be due to the contribution of grains to the electrical resistivity, and the other at lower frequencies could be due to the contribution of grain boundaries. However, the Nyquist plots for these samples show a single arc, indicating the contributions from grains and grain boundaries cannot be distinguished. This implied that the sample is electrical homogeneous [31], and the single arc was ascribed to the resistive grain boundaries. The grain boundary resistance (R_{gb}) increased with increasing sintering temperature is abnormal. It may be attributed to the co-effect of the grain size and pore, which are two competing factors that could affect the grain boundary resistance. As seen in the SEM images, both the grain size and void were enlarged when the sintering temperature increased. As the voids distance exists between the grain boundaries becomes widened could raise the energy barrier for charge transfer [32] and thus increase the grain boundary resistance. Hence, the voids distance is the dominant factor for the grain boundary resistance in which caused the grain boundary resistance to vary with the sintering temperature abnormally [33]. This anomaly trend is similar to the other report in the literature [28, 33, 34]. It is observed that the summit frequency, f_{max} of the dominant arc decreases with increasing sintering temperature. The change of summit frequency with sintering temperature has been reported elsewhere [35, 36, 37].

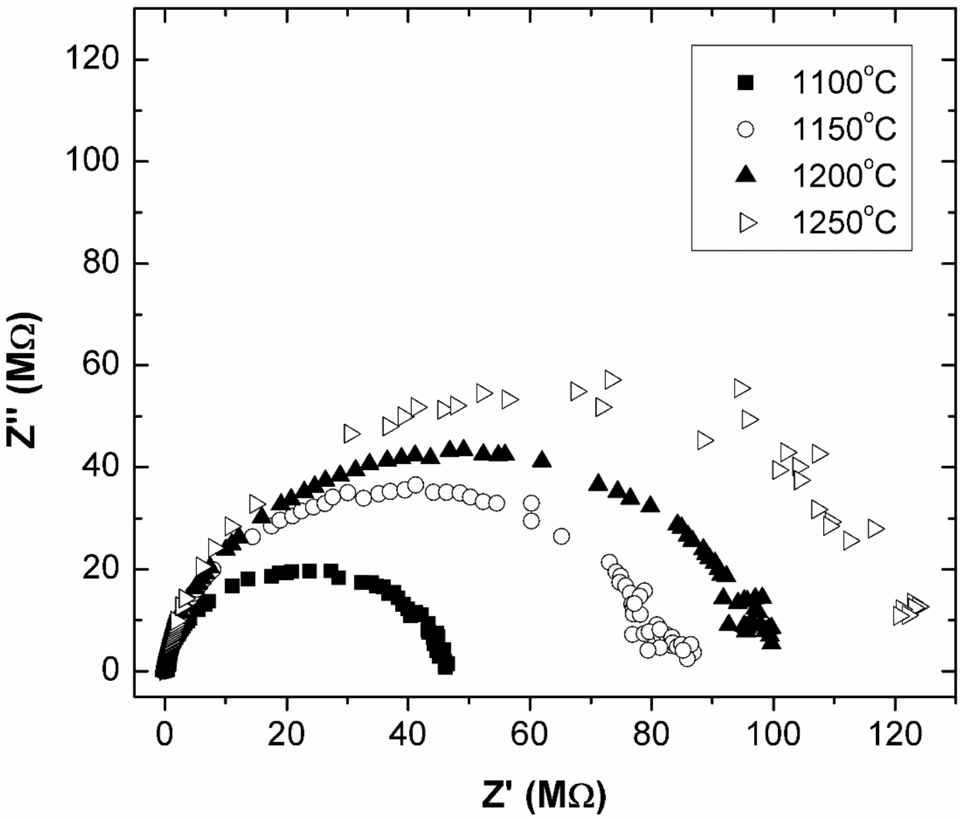

Figure 8. Nyquist plots under 300°C for calcium monosilicate sintered at different temperatures.

Figure 9 shows an alternate representation of the impedance as Z′ versus Z″/f to reveal the onset of the bulk and/or electrode terms when the Nyquist plot is dominated mainly by very resistive grain boundaries [32, 38]. From the entire impedance plot, the contribution of grain resistance (R_g), grain boundary resistance (R_{gb}) and electrode resistance (R_{el}) of the samples is observed for different sintering temperatures. There is a weak contribution in the grain region as compared to the grain boundary region. It is because ceramic materials generally have higher grain boundary resistance than grains due to the segregation of point defects at grain boundaries.

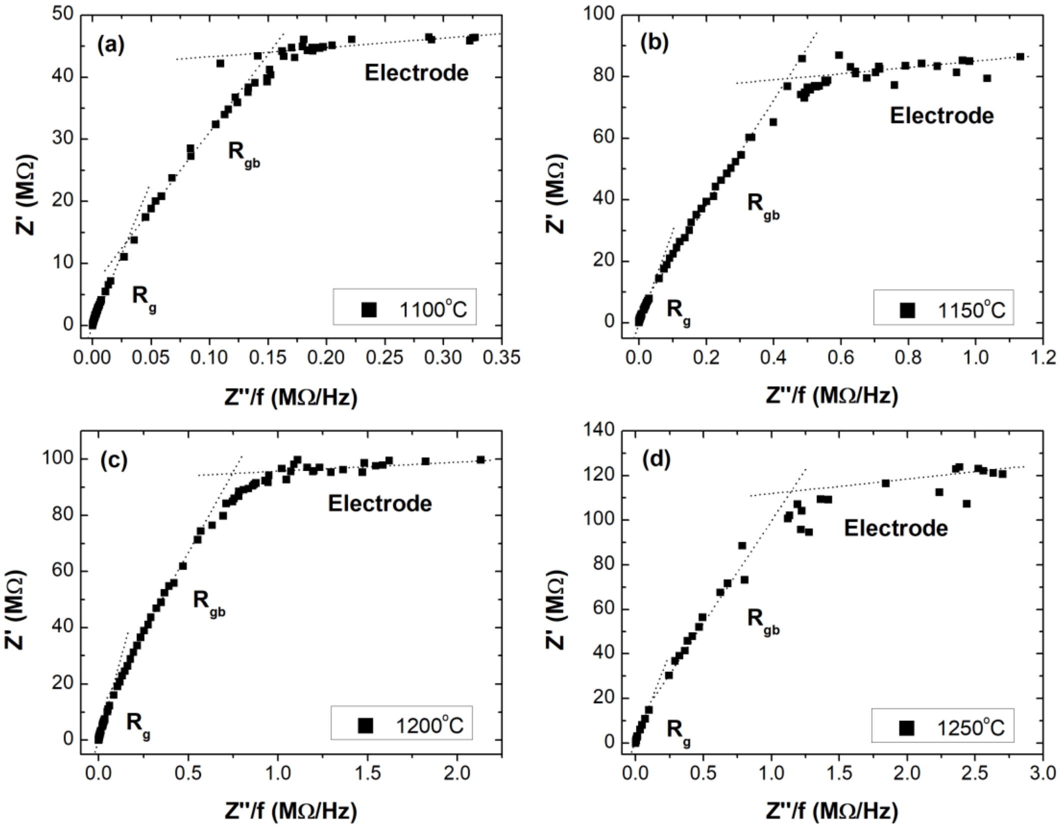

Figure 9. Alternate representations of impedance spectra under 300°C for calcium monosilicate sintered at different temperatures.

The real impedance spectrum *Z'* as a function of the frequency and sintering temperatures is plotted in Figure 10 for calcium monosilicates at 300°C. At low frequencies, the amplitude of *Z'* increases with increasing sintering temperatures mainly due to a decrease in the mobility of charge carriers and an increase in the density of trapped charges [39]. Such behaviour leads to a decrease in conductivity. This is because at higher sintering temperatures, the size of high-resistive particles increases and the density of the disordered low-resistive boundary decreases, which results in the overall enhancement of the resistive properties of the samples. In contrast, lower-temperature sintered samples have a larger number of disordered low-resistive particle boundaries and defects. This causes the charge carriers across the lattice of lower temperature sintered samples, thereby providing higher conduction and lower impedance, i.e., poor resistive nature of the samples sintered at lower temperatures [40]. In short, a larger value of impedance at a lower frequency suggests an essential role of boundaries in governing the electrical properties of the sintered ceramics. Figure 10 also shows that the *Z'* values merge and form a plateau-like behaviour for all temperatures onset of 1 kHz, indicating the increase in conductivity of the material. The low-frequency dispersion behaviour indicates the release of space charge polarization [41].

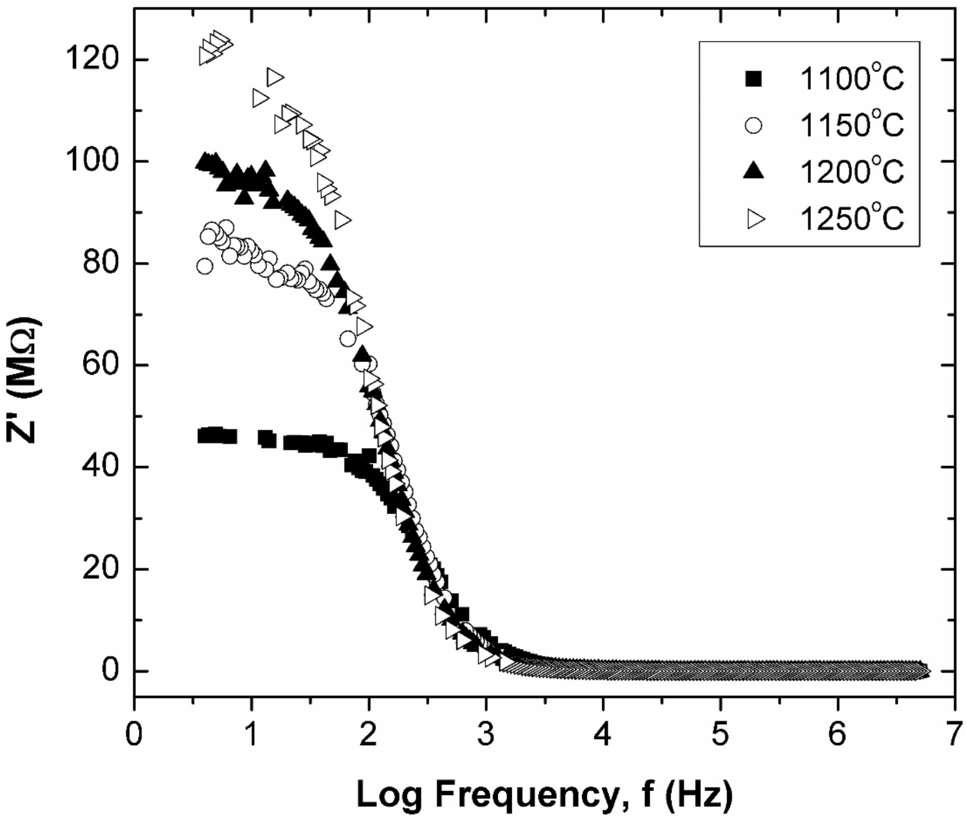

Figure 10. Variation of the real part (Z′) of impedance with frequency under 300°C for calcium monosilicate ceramics sintered at different temperatures.

Figure 11 represents the electrical conductivity spectra of calcium monosilicate at 300°C in the frequency range between 4 Hz and 5 MHz. It is clear from the plot that the range of low-frequency conductivity plateau decreases with sintering temperature, while the temperature dependency is less prominent in the high-frequency region. The conductivity increases throughout the frequency range studied is a typical conduction mechanism observed in ceramic materials. The conductivity is found to be frequency independent in the low-frequency regime indicating the contributions of long-range transport. The AC electrical response in the intermediate-frequency and high-frequency region denotes the grain boundary and grain effect, respectively [42]. As seen in Figure 11, when the sintering temperature increases from 1100°C to 1250°C, the total conductivity at 300°C increases about three orders of magnitude, reaching about 2.96×10^{-4} S/m for the sample sintered at 1250°C. Overall, the conductivity values of these samples are almost at the same level above 100 kHz, while the conductivity significantly decreases below 100 kHz as the sintering temperature increases. The pellets sintered at 1250°C exhibited a lower value of 2.1×10^{-7} S/m, as compared with the sintering temperature of 1100°C.

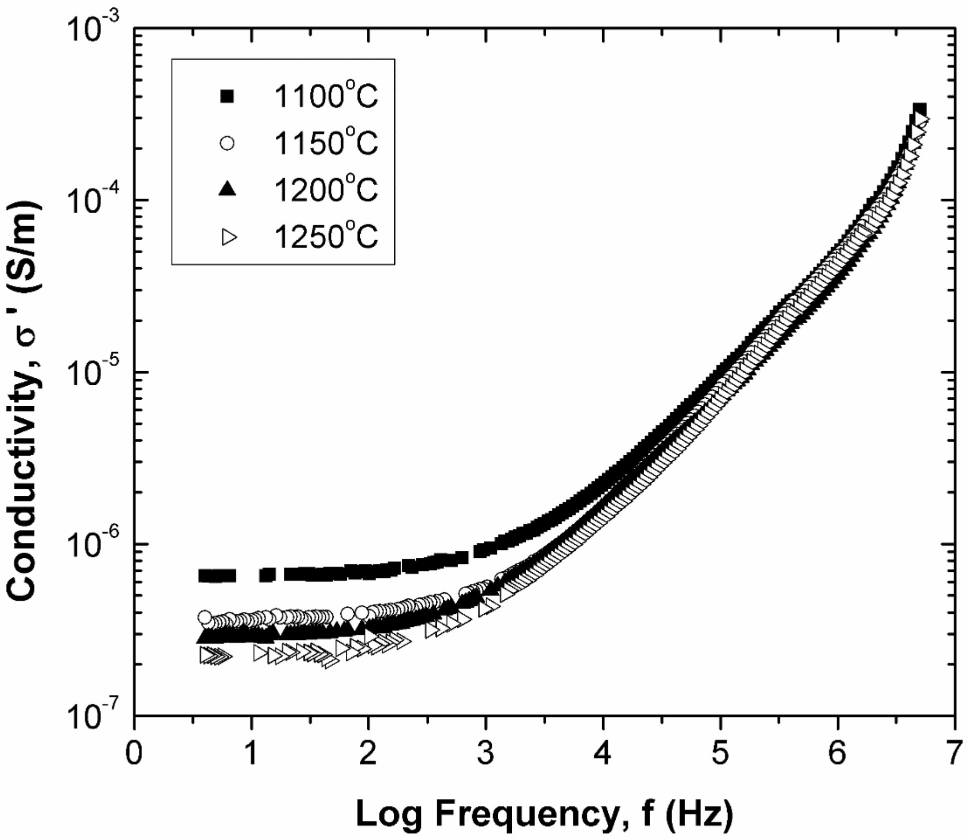

Figure 11. Frequency dependence of AC conductivity under 300°C for calcium monosilicate sintered at different temperatures.

The decrease in conductivity is greatly affected by the grain boundary resistance (R_{gb}), which is contributed by ionic transport across or along the interface area. It is well known that ionic transport is closely related to the interface area and particle size [43]. The electrical conductivity combined with the SEM result provided direct and strong evidence for interfacial conducting. It can be seen from the SEM morphology that the pellet sintered at 1250°C shows the formation of bulk structure and the reduction of interface area, and the voids distance around the grain boundary become wider. Such behaviour provides a smaller defect distribution surface area, resulting in fewer transport pathways in the structure and higher resistance to the transport of charge carriers [26, 27]. Consequently, ionic conduction in the low-frequency range is reduced. The conductivity performance gradually decreases with sintering temperatures is similar to the work from [40, 43, 44].

The dc conductivity (σ_{dc}) calculated from fitting the Jonscher's power law to the experimental data was then used to calculate the activation energy of the conduction of calcium monosilicate ceramics by using Arrhenius plot. Figure 12 shows an Arrhenius plot of pellets sintered at 1100°C to 1250°C to estimate the activation energy. The activation energy was calculated using Equation (6):

$$\sigma_{dc} = \sigma_o \exp(-E_a/K_B T) \quad (6)$$

where σ_o is the pre-exponential factor, K_B is the Boltzmann's constant, and E_a is the electrical activation energy of the conduction. The Arrhenius plot shows the linear relation from those samples, disclosing that the mechanism of conduction does not change in the temperature range of 200°C – 300°C. As seen in Figure 12, the pellet sintered at 1100°C attained the highest conductivity performance and reached a maximum value of 6.37 x 10^{-7} S/m at 300°C. The high conductivity may come from the grains with a broad size distribution, and intimate contact possessed a larger interface region between particles which provided a greater pathway for charge transfer. Thus, the interfacial ion conduction was promoted and resulted in good electrical conductivity. Furthermore, the plots show that the activation energy is about 0.98 eV, 0.89 eV, 0.96 eV, and 0.78 eV for the samples sintered at 1100°C, 1150°C, 1200°C, and 1250°C, respectively. The decrease in the activation energy is associated with reducing in the number of grains due to densification. This causes the density of the disordered low-resistive boundary to decrease upon grain growth. The decrease of activation energy with the increase of sintering temperature has also been observed by [43, 45, 46, 47]. In short, the activation energy is subjected to the microstructure and correlates with the sintering temperature.

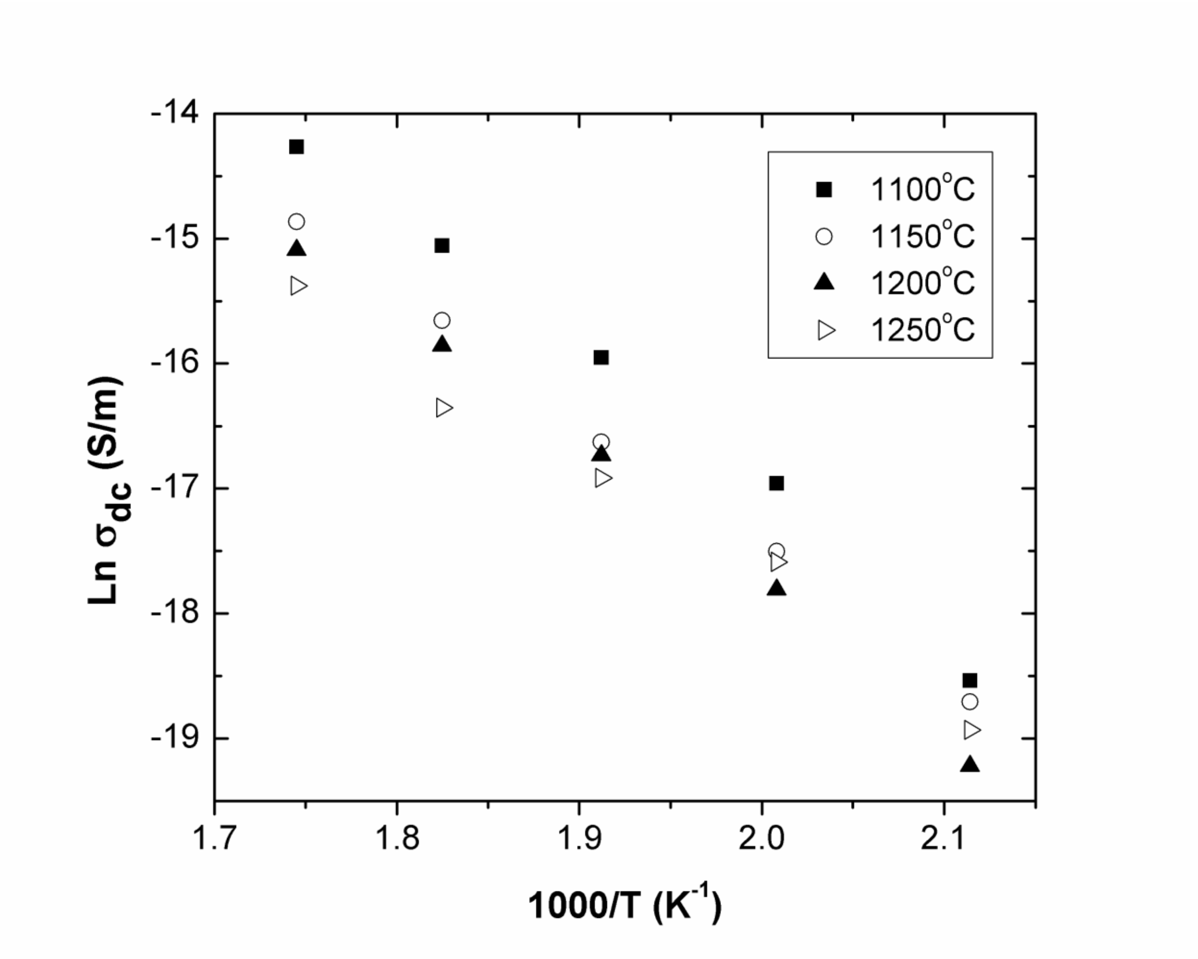

Figure 12. Arrhenius plots for the samples sintered at 1100°C – 1250°C.

4. CONCLUSION

Calcium monosilicate sintered body was successfully synthesised by mixing silica (SiO_2) and calcium oxide (CaO) derived from rice husk and eggshell in a 1:1 molar ratio through solid-state reaction. The empirical results show that as the sintering temperature increases, the phase composition of the calcium silicate sinter has minor changes, and the compactness, porosity and microstructure were also improved. It was observed that pseudo-wollastonite (α-wollastonite) was composed during the sintering process, which has better densification and lower porosity percentages. The SEM images indicate that high-temperature sintering significantly decreases the specific area and particle interfaces, and broader porosity between grain boundaries results in higher resistance for charge carriers transportation, thereby reducing the conductivity performance. Therefore, interfacial ionic conduction plays a central role in the electrical properties of calcium monosilicate ceramics. In addition, it is feasible to recycle these biological wastes to produce calcium monosilicate ceramics and lead to economic and sustainable ceramic production.

ACKNOWLEDGEMENTS

The author would like to acknowledge the support from the Fundamental Research Grant Scheme (FRGS) under a grant number of FRGS/1/2018/STG07/UNIMAP/02/2) from the Ministry of Higher Education Malaysia, and Universiti Malaysia Perlis (UniMAP) for providing the research facilities. The authors also would like to thank Poh Seng Rice Mill & Co. Sdn. Bhd. for providing the rice husks.

REFERENCES

[1] F. H. G. Leite, T. F. Almeida, R. T. Faria & J. N. F. Holanda, Synthesis and characterisation of calcium silicate insulating material using avian eggshell waste, Ceram. Int. 43, (2017) pp. 4674–4679.

[2] R. A. Bakar, R. Yahya, S. N. Gan, Production of High Purity Amorphous Silica from Rice Husk, Procedia Chem. 19, (2016) pp. 189–195.

[3] A. T. Quitain, A. T. N. Sato, H. Daimon, K. Fujie, Qualitative investigation on hydrothermal treatment of hinoki (Chamaecyparis obtusa) bark for production of useful chemicals, J. Agric. Food Chem. 51, (2003) pp. 7926.

[4] L. B. de Paiva, F. A. Rodrigues, Productive use of agricultural residues: cements obtained from rice hull ash, in: E. Lichtfouse, J. Schwarzbauer, D. Robert (Eds.), Environmental Chemistry, Springer, Berlin, (2005), pp. 621–629.

[5] M. Shahnani, M. Mohebbi, A. Mehdi, A. Ghassempour, H. Y. Aboul-Enein, Silica microspheres from rice husk: A good opportunity for chromatography stationary phase. Ind. Crops and Prod. 121, (2018) pp. 236–240.

[6] S. R. Khan, S. Jamil, M. R. S. A Janjua, Radiation assisted synthesis of dumb bell shaped calcium hydroxide nanostructures from eggshells and study of its thermal and catalytic applications. Chem. Phys. Lett. 710, (2018) pp. 45–53.

[7] M. M. Haslinawati, K. A. Matori, Z. A. Wahab, H. A. A. Sidek, A. T Zainal, Effect of temperature on ceramic from rice husk ash, Int. J. of Basic Appl. Sci. 9, (2009) pp. 22-25.

[8] T. Zaman, M. S. Mostari, M. A. Al Mahmood, M. S. Rahman, Evolution and characterisation of eggshell as a potential candidate of raw material, CerâMica, 64, (2018) pp. 236–241.

[9] J. A. Santana Costa, C. M. Paranhos, Systematic evaluation of amorphous silica production from rice husk ashes, J. Clean. Prod. 192, (2018) pp. 688–697.

[10] N. Tangboriboon, T. Khongnakhon, S. Kittikul, R. Kunanuruksapong, A. Sirivat, An innovative $CaSiO_3$ dielectric material from eggshells by sol–gel process. J. Sol-gel Sci. Technol. 58, (2011) pp. 33-41.

[11] M. B. Berger, The Importance and Testing of Density/Porosity/Permeability/Pore size for Refractories. The Southern African Institute of Mining and Metallurgy Refractories 2010 Conference, (2010) pp. 110-116.

[12] M.M. Shukur, E.A. Al-majeed, M.M. Obied, Characteristic of Wollastonite Synthesized from Local Raw Materials, Int. J. Eng. Technol. 4, (2014) pp. 426–429.

[13] D. E. Tchinda Mabah, H. K. Tchakouté, C. H. Rüscher, E. Kamseu, A. Elimbi, C. Leonelli, Design of low cost semi-crystalline calcium silicate from biomass for the improvement of the mechanical and microstructural properties of metakaolin-based geopolymer cements, Mater. Chem. Phys. 223, (2019) pp. 98–108.

[14] R. Rohim, R. Ahmad, N. Ibrahim, N. Hamidin, C. Z. Azner Abidin, Characterization of calcium oxide catalyst from eggshell waste, Adv. Environ. Biol. 8, (2014) pp. 35–38.

[15] U. Anjaneyulu, S. Sasikumar, Bioactive nanocrystalline wollastonite synthesized by sol-gel combustion method by using eggshell waste as calcium source, B. Mater. Sci. 37, (2014) pp. 207–212.

[15] D. Demir, S. Ceylan, F. Öfkeli, D. Şen, N. Bölgen Karagülle, Eggshell Derived Nanohydroxyapatite Reinforced Chitosan Cryogel Biocomposites for Tissue Engineering Applications, Jotcsb, 1, (2017) pp. 77–88.

[16] D. Demir, S. Ceylan, F. Öfkeli, D. Şen, N. Bölgen Karagülle, Eggshell Derived Nanohydroxyapatite Reinforced Chitosan Cryogel Biocomposites for Tissue Engineering Applications, Jotcsb, 1, (2017) pp. 77–88.

[17] Mirghiasi, Zahra, Fereshteh Bakhtiari, Esmaeel Darezereshki, Preparation and Characterization of CaO Nanoparticles from $Ca(OH)_2$ by Direct Thermal Decomposition Method, J. Ind. Eng. Chem. 20, (2014) pp. 113–17.

[18] Nadia Razali, Fittina Musa, Nurriswin Jumadi, Adlin Jalani, Production of Calcium Oxide from Eggshell: Study on Calcination Temperature, Raw Weight and Contact Time, RSU International Research Conference, (2021).

[19] Ozcan Dursun Can, Development of a sorbent for carbon dioxide, Graduate Theses and Dissertations, Iowa State University, (2010) pp. 11357.

[20] S. Lin, T. Kiga, Y. Wang, K. Nakayama, Energy analysis of $CaCO_3$ calcination with CO_2 capture, Energy Procedia 4, (2011) pp. 356-361.

[21] Yuliya Kan, Alexei I. Salimon, Philipp V. Sapozhnikov, Pavel A. Somov, Joris Everaerts, Alexander M. Korsunsky, On the Fabrication of Diatomite Earth-based Ceramics with Multiscale Porosity, Proceedings of the International MultiConference of Engineers and Computer Scientists 2019 (IMECS 2019), March 13-15, (2019) pp. 310-317.

[22] S. D. Souza, J. S. Visco, L. C. De Jonghe, Thin-film solid fuel cell with high performance at low-temperature, Solid State Ion. 98, (1997) pp. 57–61.

[23] S. P. Simner, J. F. Bonnett, N. L. Canfield, K. D. Meinhardt, J. P. Shelton, V. L. Sprenkle, J. W. Stevenson, Development of lanthanum ferrite SOFC cathodes, J. Power Sources, 113, (2003) pp. 1–10.

[24] R. Sagar, R. L. Raibagkar, Complex impedance and modulus studies of cerium doped barium zirconium titanate solid solution, J. Alloys Compd. 549, (2013) pp. 206–212.

[25] J. M. Debierre, P. Knauth, G. Albinet, Enhanced conductivity in ionic conductor-insulator composites: experiments and numerical model, Appl. Phys. Lett. 71, (1997) pp. 1335–1337.

[26] X. Li, X. Cao, L. Xu, L. Liu, Y. Wang, C. Meng, Z. Wang, High dielectric constant in Al-doped ZnO ceramics using high-pressure treated powders, J. Alloys Compd. 657, (2016) pp. 90–94.

[27] M. Hakamada, T. Kuromura, Y. Chen, H. Kusuda, M. Mabuchi, Influence of Porosity and Pore Size on Electrical Resistivity of Porous Aluminum Produced by Spacer Method, Mater. Trans. 48, (2007) pp. 32-36.

[28] S. Ibadat, M. Younas, S. Shahzada, M. Nadeem, T. Ali, M. Javed Akhtar, S. Pollastri, U. Rehman, I. Yousef, R. T. Ali Khan, Realistic dielectric response of high temperature sintered ZnO ceramic: a microscopic and spectroscopic approach, RSC Adv. 10, (2020) pp. 30451-30462.
[29] M. Pastor, Synthesis, structural, dielectric and electrical impedance study of Pb (Cu1/3Nb2/3) O3, J. Alloys Compd. 463, (2008) pp. 323-327.
[30] A. Chandra Bose, P. Thangadurai, S. Ramasamy, B. Purniah, Impedance spectroscopy and DSC studies on nanostructured SnO2, Vacuum 77, (2005) pp. 293-300.
[31] R. R. Raut, P. H. Salame, J. T. Kolte, C. S. Ulhe, P. Gopalan, Giant dielectric response and magnetoelectric behavior of 95BiFeO3–5BaTiO3 (95BFO–5BT) ceramics, J. Mater. Sci.: Mater. Electron. 27, (2015) pp. 730-737.
[32] J. C. C. Abrantes, J. A. Labrincha, J. R. Frade, An alternative representation of impedance spectra of ceramics, Mater. Res. Bull. 35, (2000) pp. 727-740.
[33] J. Xia, Q. Zhao, B. Gao, A. Chang, B. Zhang, P. Zhao, R. Ma, Sintering temperature and impedance analysis of Mn0.9Co1.2Ni0.27Mg0.15Al0.03Fe0.45O4 NTC ceramic prepared by W/O microemulsion method, J. Alloys Compd. 617, (2014) pp 228-234.
[34] X. Xie, J. Wang, L. Chen, Z. Hu, S. Yan, A. Chang, Effect of sintering temperature on thermal stability of Zn0.2Fe1.05NiMn0.75O4 ceramic materials by homogeneous co-precipitation method, J. Mater. Sci: Mater. Electron. 28, (2016) pp. 190–196.
[35] F. van Heuveln, H. J. M. Bouwmeester, Electrode Properties of Sr-Doped LaMnO3 on Yttria-Stabilized Zirconia: II. Electrode Kinetics, J. Electrochem. Soc. 144, (1997) pp. 134.
[36] A. Mitterdorfer, L. J. Gauckler, La2Zr2O7 formation and oxygen reduction kinetics of the La0.85Sr0.15MnyO3, O2(g)|YSZ system, Solid State Ion. 111, (1998) pp. 185-218.
[37] P. Holtappels, M. J. Jørgensen, S. Primdahl, M. Mogensen, C. Bagger, Electrochemical performance and structure of composite (La0.85Sr0.15)0.9MnO3/YSZ cathodes, in Proceedings of the Third European SOFC Forum, France, (1998), in: P. Stevens (Ed.), pp. 311.
[38] C. Jagadeeshwaran, R. Murugaraj, Investigation on structural, optical, and electrical properties for sintered Mg–Zn aluminate systems, J. Mater. Sci.: Mater. Electron. 31, (2020) pp. 6744–6754.
[39] J. Hu, H. Qin, Giant magnetoimpedance effect in La0. 7Ca0.3MnO3 under low magnetic fields, J. Magn. Magn. Mater. 231, (2001) pp. 1-3.
[40] Z. Joshi, D. Dhruv, K. N.Rathod, H. Boricha, K. Gadani, D. D. Pandya, A. D. Joshi, P. S. Solanki, N. A. Shah, Low field magnetoelectric studies on sol–gel grown nanostructured YMnO3 manganites, Prog. Solid. State Ch. 49, (2018) pp. 23-36.
[41] S. Gopukumar, Y. Jeong, K. B. Kim, Synthesis and electrochemical performance of tetravalent doped LiCoO2 in lithium rechargeable cells, Solid State Ion. 159, (2003) pp. 223-232.
[42] E. Barsoukov, J. R. Macdonald, Impedance spectroscopy: theory, experiment, and applications, John Wiley & Sons, (2018).
[43] X. Nie, Y. Chen, N. Mushtaq, S. Rauf, B. Wang, W. Dong, X. Wang, H. Wang, B. Zhu, The sintering temperature effect on electrochemical properties of Ce0.8Sm0.05Ca0.15O2-δ (SCDC)-La0.6Sr0.4Co0.2Fe0.8O3-δ (LSCF) heterostructure pellet, Nanoscale Res. Lett. 14, (2019) pp. 1-11.
[44] M. C. Martin, M. L. Mecartney, Grain boundary ionic conductivity of yttrium stabilized zirconia as a function of silica content and grain size, Solid State Ion. 161, (2003) pp. 67–79.

[45] A. B. Naik, J. I. Powar, Dependence of resistivity and activation energy of Ni-Zn ferrites on sintering temperature and porosity, Indian J. Pure and Appl. Phys. 23, (1985) pp. 436-437.

[46] S. Kazlauskas, A. Kezˇionis, T. Sˇalkus, A. F. Orliukas, Effect of sintering temperature on electrical properties of gadolinium-doped ceria ceramics, J. Mater. Sci. 50, (2015) pp. 3246–3251.

[47] H. Baaziz, N. K. Maaloul, A. Tozri, H. Rahmouni, S. Mizouri, K. Khirouni, E. Dhahri, Effect of sintering temperature and grain size on the electrical transport properties of La0.67Sr0.33MnO3 manganite, Chem. Phys. Lett. 640, (2015) pp. 77–81.